Paleoceanography and Paleoclimatology

RESEARCH ARTICLE
10.1029/2024PA004913

Special Collection:
Illuminating a Warmer World: Insights from the Paleogene

Global Warming and Equatorial Atlantic Paleoceanographic Changes During Early Eocene Carbon Cycle Perturbation V

Anne H. Kegel[1], Chris D. Fokkema[1], Henk Brinkhuis[1,2], Ursula Röhl[3], Thomas Westerhold[3], Claudia Agnini[4], Peter K. Bijl[1], Francien Peterse[1], and Appy Sluijs[1]

[1]Department of Earth Sciences, Faculty of Geoscience, Utrecht University, Utrecht, The Netherlands, [2]Department of Ocean Systems Research (OCS), Royal Netherlands Institute for Sea Research (NIOZ), Den Burg, The Netherlands, [3]MARUM - Center for Marine Environmental Sciences, University of Bremen, Bremen, Germany, [4]Dipartimento di Geoscienze, Universita degli Studi di Padova, Padova, Italy

Abstract A series of transient global warming events ("hyperthermals") in the early Eocene is marked by massive environmental and carbon cycle change. Among these events, the impacts of the Paleocene Eocene Thermal Maximum (~56 Ma), Eocene Thermal Maximum 2 (~54 Ma) and Eocene Thermal Maximum 3 (~53 Ma) are relatively well documented. However, much less is known about the many subsequent hyperthermals that apparently occurred on orbital eccentricity maxima until at least the end of the Early Eocene Climatic Optimum (EECO; ~53–49 Ma). Ocean Drilling Program (ODP) Site 959 (Equatorial Atlantic Ocean), we report a large negative carbon isotope excursion (CIE) in both organic and carbonate substrates that we correlate to the "V" event *sensu* Lauretano et al. (2016), https://doi.org/10.1127/nos/2016/0077 (or C22nH1 *sensu* Sexton et al. (2011), https://doi.org/10.1038/nature09826) at ~49.7 Ma, following combined bio- and chemostratigraphic constraints. Through TEX_{86} paleothermometry, we reconstruct a sea surface temperature rise of 1.3–2.0°C associated with this CIE, which, combined with evidence for warming from the deep sea, implies that this event indeed represents a transient global-scale warming episode like the earlier hyperthermals. Organic walled dinoflagellate cyst assemblages indicate a productive paleoceanographic background setting, likely through regional upwelling, which alternated with episodes of stratification. Warming reconstructed across V at Site 959 is relatively similar to the higher-latitude-derived deep ocean reconstructions. However, the presence of upwelling and its variable intensity across the event compromises the use of the reconstructed warming as an estimate for the complete tropical band.

Key Points:

- Equatorial sea surface and deep ocean warming marked early Eocene carbon isotope excursion V, implying it was a global warming event
- A longer isotope recovery in organic compared to inorganic carbon suggests a contribution of older dissolved organic carbon at Site 959
- Dinoflagellate cysts indicate a productive setting related to upwelling that commenced since the end of the Early Eocene Climatic Optimum

Supporting Information:

Supporting Information may be found in the online version of this article.

Correspondence to:

C. D. Fokkema,
c.d.fokkema@uu.nl

Citation:

Kegel, A. H., Fokkema, C. D., Brinkhuis, H., Röhl, U., Westerhold, T., Agnini, C., et al. (2025). Global warming and equatorial Atlantic paleoceanographic changes during early Eocene carbon cycle perturbation V. *Paleoceanography and Paleoclimatology*, *40*, e2024PA004913. https://doi.org/10.1029/2024PA004913

Received 16 APR 2024
Accepted 23 NOV 2024

1. Introduction

Persistent deep ocean warming during the late Paleocene and early Eocene climaxed at the end of the Early Eocene Climatic Optimum (EECO; ~53–49 Ma) (Shackleton, 1986; Westerhold et al., 2020). This trend is mimicked by sea surface temperature (SST) reconstructions in both low and middle, and high latitudes, indicating that they represent global mean surface temperature (GMST) variability (e.g., Bijl et al., 2009; Cramwinckel et al., 2018; Gaskell et al., 2022; Hollis et al., 2012). During the EECO, GMSTs were approximately 10–16°C elevated relative to pre-industrial temperatures (Inglis et al., 2020) and atmospheric CO_2 concentrations exceeded 1,000 ppmv (Anagnostou et al., 2020).

Superimposed on this long-term trend, approximately 20 transient negative stable carbon ($\delta^{13}C$) isotope excursions (CIEs) occurred in the ocean-atmosphere system (Agnini et al., 2009; Cramer et al., 2003; Frieling et al., 2018; Kennett & Stott, 1991; Kirtland Turner et al., 2014; Lauretano et al., 2018; Littler et al., 2014; Lourens et al., 2005; Sexton et al., 2011). These transient CIEs and associated deep ocean carbonate dissolution horizons reflect the rapid and massive injection of ^{13}C-depleted carbon from outside the global exogenic carbon reservoir pool into the ocean-atmosphere system (Dickens et al., 1995, 1997). Most, or all of these events, are paced by eccentricity cycles of ~100- and ~405-kyrs (Cramer et al., 2003; Galeotti et al., 2010; Lauretano et al., 2016; Laurin et al., 2016; Littler et al., 2014; Lourens et al., 2005; Piedrahita et al., 2022; Westerhold et al., 2017, 2018; Zachos et al., 2010). This view is recently strengthened by a recorded loss in resilience in climate-carbon cycle dynamics leading up to the events (Setty et al., 2023). The coeval negative excursions in benthic foraminiferal oxygen isotope ratios ($\delta^{18}O$) are interpreted to reflect deep ocean warming (Kennett & Stott, 1991; Lauretano et al., 2018; Lourens et al., 2005). SST proxy records indicate that at least a great part of these events indeed represent global warming events (Dunkley Jones et al., 2013; Fokkema et al., 2024;

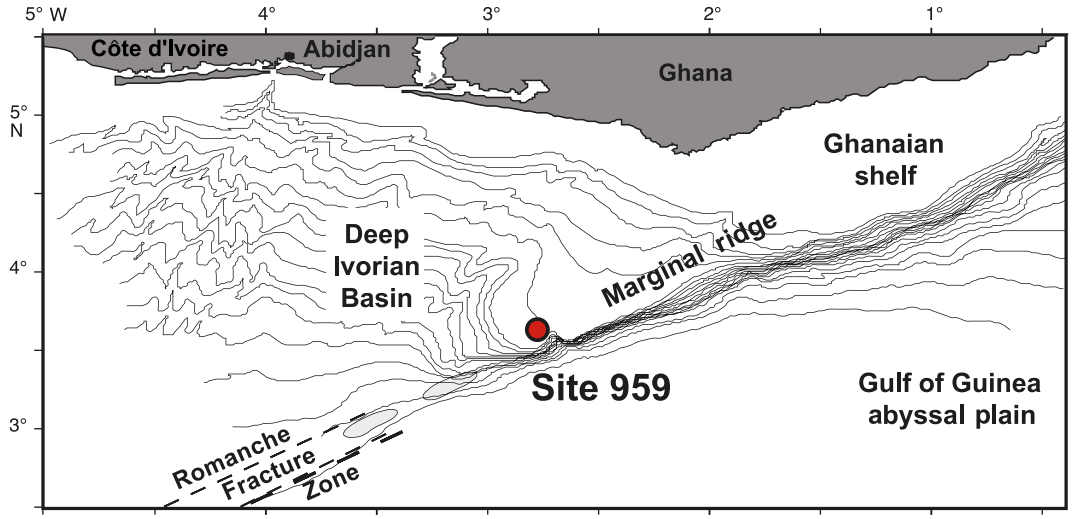

Figure 1. Present day location of ODP Site 959 in the eastern equatorial Atlantic Ocean. Map adapted from Mascle et al. (1996).

Frieling et al., 2018; Lourens et al., 2005; Sluijs et al., 2009) and can therefore be termed "hyperthermals" (Thomas & Zachos, 2000). However, the exact driving mechanisms and carbon sources are still under debate (e.g., Frieling et al., 2019). Potential external carbon sources can include (a combination of) methane hydrates and terrestrial organic carbon (DeConto et al., 2012; Dickens et al., 1995; Kurtz et al., 2003). Volcanic sources may have contributed to carbon injection during the largest hyperthermal, the Paleocene-Eocene Thermal Maximum (PETM; ~56 Ma; e.g., Svensen et al., 2004; Frieling et al., 2019; Berndt et al., 2023).

The PETM is associated with massive environmental and concomitant biotic change on land and in the ocean (Hupp et al., 2022; McInerney & Wing, 2011; Sluijs et al., 2007). Some of the subsequent lesser hyperthermals are regionally associated with biotic changes as well, notably Eocene Thermal Maximum 2, and Eocene Thermal Maximum 3, but others, where documented, show little to no change (Agnini et al., 2009; Gibbs et al., 2012; Rush et al., 2023; Sluijs et al., 2009; Willard et al., 2019). In contrast, it has been proposed that in some tropical regions during the PETM, fossil organic walled dinoflagellate cyst (dinocyst) and planktic foraminifer assemblages suggest the disappearance of eukaryotic plankton because of heat stress, when warming led to temperatures near thermo-physiological limits, or the rate of warming resulted in reduced prevalence and biodiversity (Aze et al., 2014; Frieling et al., 2017, 2018).

So far, most studies focused on the early set of hyperthermals, whereas the events that occurred during the later part of the EECO received much less attention (Kirtland Turner et al., 2014; Sexton et al., 2011; Westerhold et al., 2017, 2018). Consequently, while for a series of the earlier hyperthermals (PETM–L2, ~56–52.4 Ma) surface ocean warming has been reconstructed in multiple regions including the tropics (Fokkema et al., 2024; Frieling et al., 2017, 2018; Sluijs et al., 2009), evidence for warming of hyperthermals during the later part of the EECO (~52–49 Ma) is limited to negative excursions in benthic foraminiferal $\delta^{18}O$ (Westerhold et al., 2018), that presumably reflects Southern Ocean SST variability (Hollis et al., 2012; Zhang et al., 2022). In addition, to our knowledge, no studies of biotic change have been carried out for these later perturbations.

Therefore, here we aim to evaluate temperature and ecological variability across the later part of the EECO in sediments recovered at Ocean Drilling Program (ODP) Site 959, located in the Equatorial Atlantic (Figure 1). Previous Eocene reconstructions on Site 959 using TEX_{86} (TetraEther indeX of tetraethers consisting of 86 carbon atoms; Schouten et al., 2002) paleothermometry have demonstrated that the PETM was associated with ~3°C warming, and hyperthermals I1–L2 with ~1–1.5°C from baseline temperatures exceeding 33°C (Fokkema et al., 2024; Frieling et al., 2019). We follow up on this work by searching for CIEs using stable carbon isotope analyses on a late-EECO interval of Site 959. We constrain the chronostratigraphy using the available biostratigraphic data and identify hyperthermal related variability in the record. Then, we assess environmental and biotic changes over the interval using TEX_{86} and palynological associations.

2. Material and Methods

2.1. Ocean Drilling Program Site 959

ODP Leg 159 Site 959 (3.62760° N, 2.735817° W) is located ∼140 km offshore of Ghana in the eastern equatorial Atlantic Ocean at a depth of 2,100 m on the northern slope of the Côte d'Ivoire-Ghana Marginal Ridge, which divides the Deep Ivorian Basin from the abyssal plain of the Gulf of Guinea (Mascle et al., 1996) (Figure 1). Site 959 has accumulated sediments with ample organic matter since the Late Cretaceous (Wagner, 2002), which has allowed for low latitude paleoclimate reconstructions by lipid biomarkers and organic walled dinoflagellate cysts (dinocysts) throughout the Cenozoic Era (e.g., Cramwinckel et al., 2018; van der Weijst et al., 2022). The lower Eocene sediments, consisting of clay-bearing chalks and porcellanites (Mascle et al., 1996), were deposited at a paleolatitude of ∼9° S (http://paleolatitude.org, *model version 2.1* (van Hinsbergen et al., 2015); using the paleomagnetic reference frame of Torsvik et al. (2012)). An open marine depositional environment during the early Eocene was inferred by previous work based on the (near) absence of terrestrial palynomorphs and dominance of dinocyst taxa typical for outer shelf to open marine environments (Fokkema et al., 2024). The appearance of heterotrophic dinocysts and increased total organic carbon (TOC) content around the end of the early Eocene (∼49 Ma) suggests the onset, or intensification of upwelling around that time (Cramwinckel et al., 2018; Fokkema et al., 2024).

2.2. Stratigraphic Framework

The PETM and CIEs I1 to L2 were previously identified in Hole D Cores 42R (Frieling et al., 2018) and 39R (Fokkema et al., 2024; Figure 2). Core 38R had very poor recovery (10%, Mascle et al., 1996). Therefore, our search for late EECO CIEs focuses on Core 37R, which has reasonable recovery (51.8%, Mascle et al., 1996) (Figure 2). Incomplete recovery around the studied interval complicates the construction of a reliable stratigraphic framework. However, the base of calcareous nannofossil *Discoaster sublodoensis* in Core 37R at 755.11 ± 0.04 mbsf (Fokkema et al., 2024) provides important constraints. However, this event is generally considered a problematic biohorizon, because: (a) this datum is reported to be relatively prone to diagenetic overgrowth (Backman, 1986), (b) the occurrences in the lower part of its range are sporadic (Backman, 1986), (c) its taxonomy is only relatively recently improved (Agnini et al., 2006) and (d) this event has an inconsistent position at Walvis Ridge ODP Sites 1265 and 1263 (Westerhold et al., 2017). Nevertheless, the use of a consistent taxonomy and the standardization of a semi quantitative counting result in a very consistent position of this event between astronomically tuned ODP Sites 1265 (Walvis Ridge, South Atlantic) and Site 1258 (Demerara Rise, equatorial Atlantic), where it is reported in the base of magnetochron C22n, between the V (49.685 Ma; C22nH1) and W (49.585 Ma; C22nH2) CIEs (Westerhold et al., 2017). The offset observed between Site 1263 and 1265 is potentially caused by core disturbance of this interval at Site 1263 (Westerhold et al., 2017). Therefore, the available data support the hypothesis that the base of *D. sublodoensis* is indeed positioned between the V and W CIEs. The calculated age of this event at Sites 1265 and 1258 is also consistent with the tuned age of this biohorizon at the Newfoundland Ridge International Ocean Discovery Program (IODP) Site U1410, although that site lacks paleomagnetic data in that interval (Cappelli et al., 2019). Collectively, we might expect to find CIEs V and/or W close to this bioevent.

2.3. Methods

For this study, we sampled the working halves of Hole 959D, Core 37R (759.5–754.5 mbsf) at 2 cm resolution at the Bremen Core Repository of the IODP. All samples were freeze-dried. Selections of samples were analyzed for magnetic susceptibility, bulk carbonate stable carbon and oxygen isotope ratios, bulk organic carbon isotope ratios, biomarkers, and palynology. Archive halves were subject to X-Ray Fluorescence (XRF) scanning.

2.3.1. Color Reflectance

Total color reflectance data was generated from the original sediment core images (Mascle et al., 1996) following the methodology described by Zeeden et al. (2015). Images were prepared by deleting cracks, drilling mud and other unconformities, and data was generated at 1-cm resolution using the R-script by Kocken (2023).

10.1029/2024PA004913

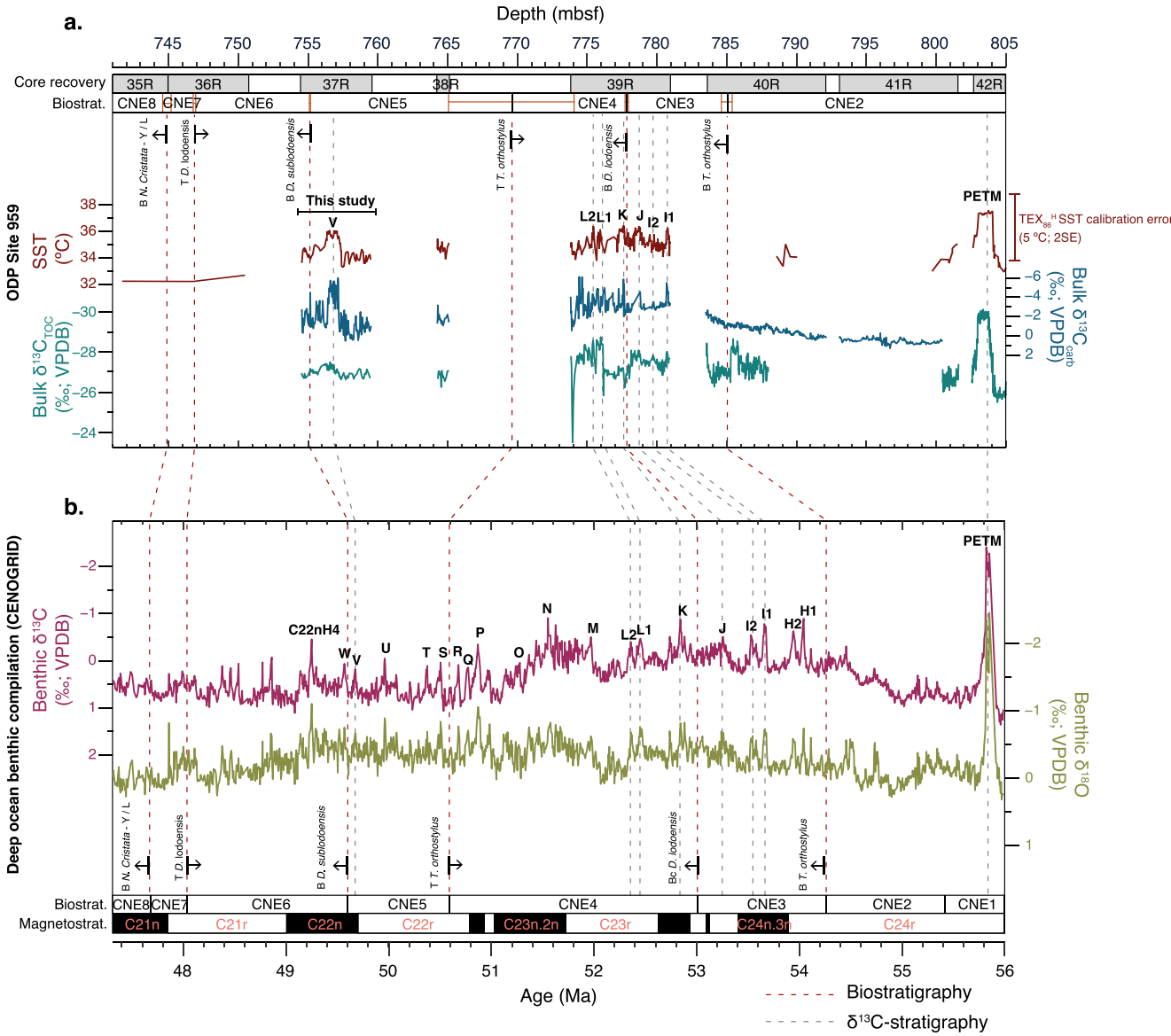

Figure 2. Stratigraphic correlation of Site 959 to a global deep ocean benthic compilation. (a) Site 959 data (TEX_{86}-based SST, bulk organic and carbonate $\delta^{13}C$, calcareous nannofossil biostratigraphy), including newly generated data for Core 37R and previously published data (Cramwinckel et al., 2018; Fokkema et al., 2024; Frieling et al., 2018, 2019). Calibration error (2SE) of the used SST transfer function is indicated by the red line on the right side of the figure. (b) Benthic foraminiferal $\delta^{13}C$ and $\delta^{18}O$ from the CENOGRID compilation (Westerhold et al., 2020). The dashed lines mark the correlations based on calcareous nannofossils (red) and CIEs (gray). The calcareous nannofossil biostratigraphic zonation (CNE zones) follows definitions by Agnini et al. (2014), and the ages are the astronomically calibrated by Westerhold et al. (2017).

2.3.2. Bulk Magnetic Susceptibility

For bulk magnetic susceptibility (MS) measurements, samples were crushed to ~0.5 cm large pieces and weighed. MS was measured with a MFK1-FA on 212 samples at Utrecht University. Each measurement was repeated at least thrice. Analytical uncertainty was smaller than 5.3×10^{-10} χ.

2.3.3. XRF Scanning

XRF Core Scanner data were collected in 2009 every 1 cm down-core over a 1.2 cm^2 area with a down-core slit size of 10 mm using generator settings of 10 kV, a current of 0.2 mA, and a sampling time of 30 s directly at the split core surface of the archive half with XRF Core Scanner III (AVAATECH Serial No. 12) at the MARUM - University of Bremen. The split core surface was covered with a 4 μm thin SPEXCerti Prep Ultralene1 foil to

avoid contamination of the XRF measurement unit and desiccation of the sediment. The here reported data have been acquired by a Canberra X-PIPS Detector (Model SXP 5C–200–1,500) with 200 eV X-ray resolution, the Canberra Digital Spectrum Analyzer DAS 1000 and an Oxford Instruments 100 W Neptune X-ray tube with rhodium (Rh) target material. Raw data spectra were processed by the analysis of X-ray spectra by Iterative least squares software (WIN AXIL) package from Canberra Eurisys.

2.3.4. Isotope Measurements

Stable carbon and oxygen isotope ratios of bulk carbonate ($\delta^{13}C_{carb}$ and $\delta^{18}O_{carb}$, respectively) were measured on powdered samples using a Thermo Finnigan GasBench II system coupled to a Thermo Delta-V isotope ratio mass spectrometer (IRMS) at Utrecht University. Results were calibrated to delta values relative to the Vienna Pee Dee Belemnite (VPDB) using an in-house carbonate standard "NAXOS" ($\delta^{13}C = 2.08‰$; $\delta^{18}O = -6.83‰$) and the international carbonate standard IAEA-CO-1. Analytical precision, based on repeated measurements of NAXOS, were better than 0.11‰ for $\delta^{18}O_{carb}$ and 0.05‰ for $\delta^{13}C_{carb}$ (1σ). For 15 samples that required relatively large amounts of sediment (>1,000 μg) due to low carbonate content, analytical uncertainty increased up to 1‰ due to H_2S formation.

For bulk organic carbon isotope ratios ($\delta^{13}C_{TOC}$), approximately 0.3 g per sample was powdered, and treated with 25 mL HCl to dissolve the carbonates. Samples were crushed after drying and analyzed on a Thermo Scientific Flash IRMS Elemental Analyzer coupled to a Thermo Scientific Delta V Advantage isotope ratio mass spectrometer. Standard bracketing using the in-house standard nicotinamide ($\delta^{13}C = -33.08‰$) allowed for calibration of delta values relative to the VPDB. Analytical precision, based on repeated measurements of the nicotinamide standard, were smaller than 0.05‰ (1σ).

2.3.5. Total Organic Carbon Content and Carbonate Weight Percentage

The $CaCO_3$ content ($CaCO_3$wt%) was approximated by two independent methods; the first estimation was based on the weight loss after decalcification with HCl, here-after referred to as "$CaCO_3wt\%_{wl}$ (see Section 2.3.4). This method presumably slightly overestimates the $CaCO_3$ content due to removal of additional material (e.g., salts). In the second method, the $CaCO_3$wt% was approximated based on the relation between the mass spectrometer m/z 44 signal intensity and mass of the weighted sediment sample, in comparison to that of the pure carbonate standards (same approach as described in Fokkema et al. (2022)) here-after referred to as "$CaCO_3wt\%_{ms}$. The precision was better than 9.5% (1σ) based on the carbonate standards.

The weight percentage of total organic carbon content (TOCwt%) was measured on the EA during $\delta^{13}C_{TOC}$ analysis. Analytical precision, based on repeated measurements of the nicotinamide standard, was better than 0.05% (1σ).

2.3.6. GDGT Analysis

For 92 samples, a subsample of ~4–16 g was powdered for the analysis of glycerol dialkyl glycerol tetraethers (GDGTs). Lipids were extracted with a mixture of dichloromethane (DCM) and MeOH (9:1, v/v) using a Milestone Ethos X Microwave extraction system (70°C; 50 min). An internal standard (99 ng of C_{46} GTGT) was added to allow for quantitative assessment of GDGT concentrations. Subsequently, solvent mixtures of hexane: DCM (9:1), hexane:DCM (1:1) and MeOH:DCM (1:1) were used to respectively separate the total lipid extract into apolar, ketone and polar fractions over an activated Al_2O_3 column. The polar fractions, containing the GDGTs, were dried under a gentle N_2 stream, redissolved in hexane:isopropanol (99:1) and filtered through a 0.45 μm polytetrafluorethylene filter, after which they were measured on an Agilent 1290 ultra-High Performance Liquid Chromatography (UHPLC) coupled to a Agilent 6135 Mass Spectrometer (MS), following the methodology as described by Hopmans et al. (2016). GDGTs were identified by detecting their $[M+H]^+$ ions in selected ion monitoring mode. Quantification was achieved by peak area integration and comparing that with the area of the internal standard, assuming that the response of the MS was similar for all compounds. A minimum signal-to-noise ratio of >3 was maintained as detection limit.

GDGT distributions were first tested for non-thermal controls on the TEX_{86} using various published ratios and indices by applying the R script of Bijl et al. (2021), resulting in exclusion of two samples (Figure S1 in Supporting Information S1). TEX_{86} values were translated to temperatures using a SST calibration (TEX_{86}^H;

Kim et al., 2010) and, because sedimentary GDGTs most likely derive from just below the mixed layer (Massana et al., 2000; Rattanasriampaipong et al., 2022; Taylor et al., 2013), also with a subsurface temperature calibration (SubT) that targets the layer between 100 and 250 m water depth ($SubT_{100–250m}$; Ho & Laepple, 2016).

Analytical precision, based on repeated analysis of an internal lab standard ($n = 4$), was smaller than 0.0015 for the TEX_{86}, which translates to 0.06°C following the TEX_{86}^{H} calibration in the range of TEX_{86} values encountered. The calibration errors (1SE) of absolute TEX_{86}-based temperature estimates are 2.5°C and 1.7°C for the used TEX_{86}^{H}-SST and SubT calibrations, respectively. Importantly, we assume that the nature of the TEX_{86}-temperature relationship remains constant within our data set. Therefore, as this work focusses on reconstruction variability of SSTs in contrast to absolute SSTs, the calibration errors are not propagated into the analyses of temperature change. Instead, the uncertainty in temperature variability is assessed by Monte Carlo propagation of the analytical errors and sample population errors. The reported error margin of ΔT includes the combined estimates of the SST and SubT calibrations to cover the plausible range of depth-depended TEX_{86}-temperature slopes in the modern system, following the approach by Fokkema et al. (2024). The significance of temperature change was assessed by an unpaired *t*-test. Reported uncertainties reflect 95% confidence intervals (95%CIs).

2.3.7. Palynology

Forty-one samples were crushed to ∼5 mm size pieces and prepared in the Palynology Lab at Utrecht University, using standard methods (e.g., Cramwinckel et al., 2018). In short, samples were treated with HCl and HF and residues were sieved over 250- and 15-µm sieves. The addition of a known number of *Lycopodium clavatum* spores prior to processing provides for quantitative assessment (Stockmarr, 1972). Microscope slides were prepared using glycerine jelly. Dinocysts were classified at genus and if possible, at species level, using the taxonomy of that cited in Williams et al. (2017). Taxa were grouped based on inferred ecological niches, following modern (Thöle et al., 2023; Zonneveld et al., 2013) and Paleogene distributions and affinities (Brinkhuis, 1994; Frieling & Sluijs, 2018; Pross & Brinkhuis, 2005; Sluijs & Brinkhuis, 2009).

3. Results

3.1. Bulk Carbonate and Bulk Organic Isotopic Compositions

3.1.1. Carbon Isotope Excursion "V"

We record a significant CIE in the $\delta^{13}C_{carb}$ and $\delta^{13}C_{TOC}$ data between ∼757.2 and 756.3 mbsf (Figures 2 and 3), with magnitudes of 3.4 and 0.6‰, respectively. The timing of recovery to background values differs between $\delta^{13}C_{carb}$ and $\delta^{13}C_{TOC}$, the rise in $\delta^{13}C_{carb}$ at 756.36 mbsf precedes that of the $\delta^{13}C_{TOC}$ by ∼55 cm. The $\delta^{18}O_{carb}$ data exhibits overall low values (mean = −4.7‰) that drop to values as low as −7.1‰ during the CIE (Figure S1 in Supporting Information S1). Although this negative oxygen isotope excursion might support the presence of a hyperthermal, such low values may also point to secondary overprint of the $\delta^{18}O$ signals. Specifically, an overprinted bulk carbonate $\delta^{18}O$ signal at Eocene Site 959 presumably results from late stage alteration during burial (Schrag et al., 1995), and a significant authigenic carbonate component is in line with pore-water analyses (Mascle et al., 1996) and previous bulk carbonate $\delta^{18}O$ analyses (Fokkema et al., 2024). Therefore, we do not further interpret $\delta^{18}O_{carb}$ as a paleoclimatic proxy indicator. Collectively, however, this CIE stands out significantly relative to background values suggesting the presence of a globally recorded CIE. The CIE occurs just below the base of *D. sublodoensis*, implying that it most likely represents the "V" CIE at 49.7 Ma (Lauretano et al., 2016) (also termed "C22nH1"; Sexton et al., 2011) (see Section 2.2; Figure 2).

3.1.2. Background $\delta^{13}C$ Variability

The $\delta^{13}C_{carb}$ ranges between ∼−2 and 0‰ from the base of Core 37R up to the V event (759.5–757.2 mbsf). Above the event (<756.3 mbsf), $\delta^{13}C_{carb}$ values recover to average values between ∼−3 and −1‰ (Figure 3). The $\delta^{13}C_{TOC}$ data shows ∼50 cm background variability between −26.7‰ and −27.2‰ surrounding V. Within the CIE, values vary between −27.5 and −27.1‰.

10.1029/2024PA004913

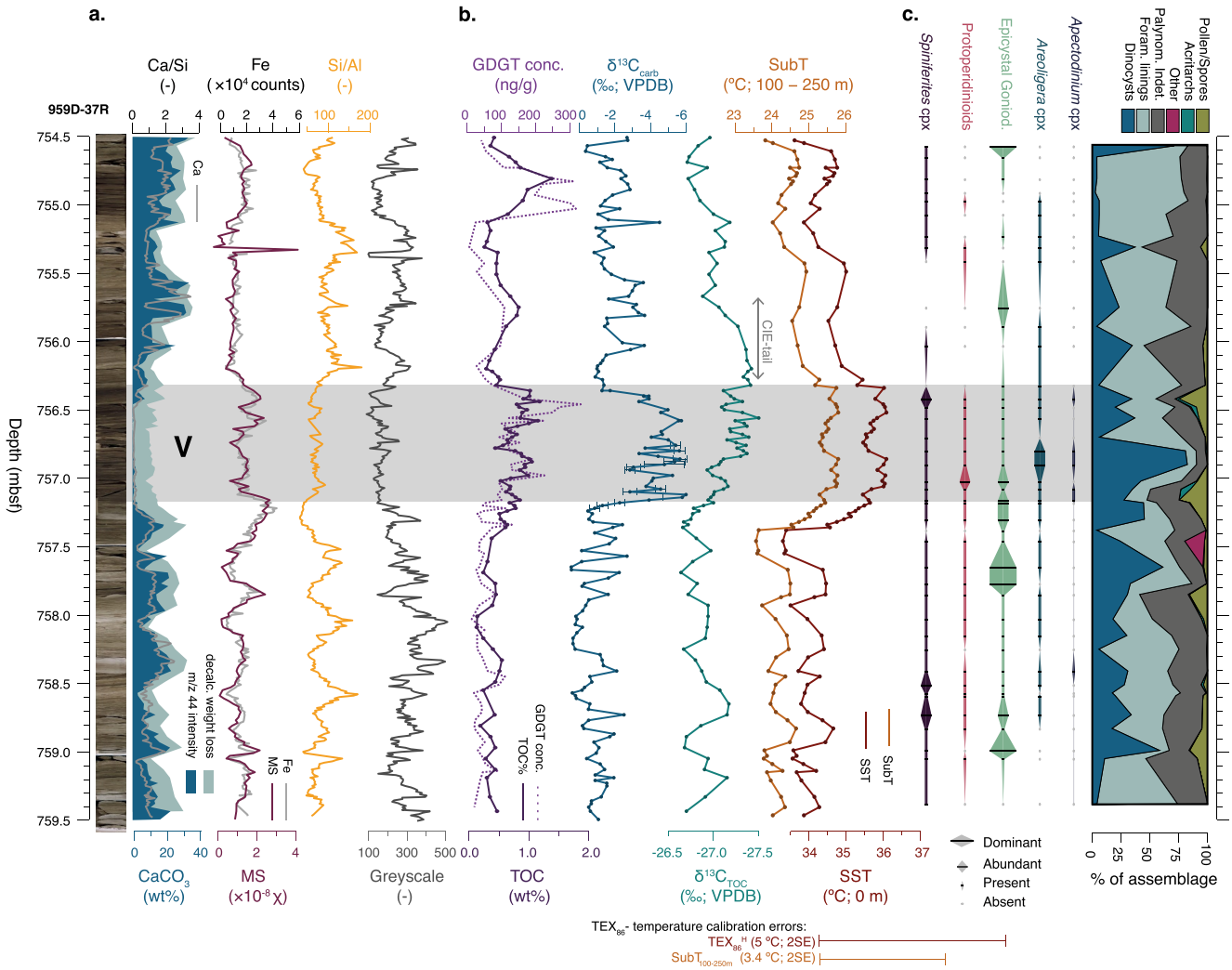

Figure 3. Downcore analysis results for Site 959D Core 37R. (a) Core photograph, two methods for $CaCO_3$wt% (dark and light blue areas, see Section 2.3.5) and Ca/Si (gray line), bulk magnetic susceptibility (MS) and XRF-based Fe counts, Si/Al, Greyscale. (b) TOCwt% and GDGT concentrations (dotted line), bulk carbonate $\delta^{13}C$, total organic $\delta^{13}C$, TEX_{86}-based SubT (orange, following the $SubT_{100–250m}$ calibration; Ho & Laepple, 2016) and SST (red, following the TEX_{86}^{H} calibration; Kim et al., 2010). Calibration errors (2SE) of the used SST and SubT transfer functions are indicated on the bottom. (c) Palynology results with semi-quantitative dinocyst assemblages and the relative abundances of constituents that make up the complete palynomorph assemblage. Dark gray band indicates the CIE horizon.

3.2. Sediment Composition

3.2.1. Core Picture and Sediment Color

Site 959D Core 37R is characterized by prominent variations in sediment color, ranging from dark brown to light gray (Figure 3). Across the complete core, the darker and lighter intervals alternate on submeter scale. An extended dark horizon marks the V event in the middle of the core between 757.2 and 756.3 mbsf, and relatively light-colored sediments mark the lower part of the section. One occurrence of a black chert at ~755.4 mbsf stands out in the core picture.

3.2.2. $CaCO_3$ and Organic Carbon Content

The two independent $CaCO_3$wt% proxies (light and dark blue areas in Figure 3a) correlate well ($R^2 = 0.87$; $p < 0.001$), but the decalcification-weight-loss method yields 5–10 wt% higher values (Figure S1 in Supporting Information S1), presumably due to the loss of non-$CaCO_3$ components during HCl treatment. The $CaCO_3wt\%_{ms}$ displays a continuous ~50 cm variability across the bottom half of the core, ranging between ~2 and 24% and

strongly declines to negligible amounts during the V event. Above this horizon, $CaCO_3$wt% rises to values of approximately 10% higher than the lower interval, varying between 10% and 34% on meter scale.

The TOCwt% varies in-phase with $CaCO_3$wt% in the top and bottom part of the interval, ranging between 0.2% and 0.6% in ~50 cm intervals in the bottom halve of the core. In the dark colored interval marking V, TOCwt% rises to higher values up to 1.2%. Above, the TOCwt% remains elevated compared to the base of the section and reaches two maxima at 755.75 and 754.75 mbsf, with values of 0.9% and 1.4%, respectively.

3.2.3. Magnetic Susceptibility

The MS values (Figure 3a) range between -3.7×10^{-9}–3.9×10^{-8} χ. Overall variability in the MS record corresponds to that of TOCwt%: showing a continuous ~50 cm variability from the base of the section to 756.36 mbsf, with relatively higher values during V. The 1-m-scale variability above the V event to the top of the section is relatively dampened. Interestingly, one high MS peak coincides with the bottom of the identified black chert, immediately followed by slightly negative MS.

3.2.4. X-Ray Fluorescence (XRF)

Ca and Si compose the bulk signal intensity of the XRF scan. Ca significantly covariates with the $CaCO_3wt\%_{ms}$ ($R^2 = 0.82$; $p < 0.001$) and $CaCO_3wt\%_{wl}$ ($R^2 = 0.73$, $p < 0.001$) (Figure S1 in Supporting Information S1). For most of the record, Si and Ca display a strong anticorrelation across regular ~50-cm-scale alternations, whereas both elements decline during V (757.4–756.4 mbsf). Interestingly, the regular occurring maxima of Si and Ca are both in the lighter core intervals. Furthermore, Fe correlates strongly with the MS, Al and K (Figure S1 in Supporting Information S1), representatives of the terrestrially derived clay component.

3.3. TEX_{86} Paleothermometry

Concentrations of isoprenoid GDGTs range between 6 and 332 ng/g throughout the core. All isoprenoid GDGTs relevant for TEX_{86} paleothermometry were above detection limit in all samples. An average GDGT-2/GDGT-3 ratio of 3.7 indicates predominant GDGT export origin from the upper top 200 m of the ocean water column (Hurley et al., 2018; Rattanasriampaipong et al., 2022; Taylor et al., 2013; van der Weijst et al., 2022). There is no clear correlation between the TEX_{86} and the GDGT-2/GDGT-3 ratio ($R^2 = 0.05$; $p = 0.026$). Branched GDGTs are absent or only present in low concentrations, hence the branched and isoprenoid tetraether (BIT) index that can indicate potential GDGT inputs from the terrestrial realm (Hopmans et al., 2004) reflects consistently very low values (<0.01), characteristic for open marine settings. Two samples show large (>0.3) deviations from the modern Ring Index-TEX_{86} relationship (Δ-RI; Zhang et al., 2016) indicating a possible non-thermal overprint on the temperature signal and were discarded (Figure S2 in Supporting Information S1).

The mean of TEX_{86}^{H}-based SSTs in the interval prior to V is 34.0 (+34.5/−33.3) ºC, with SubTs of 24.1 (+24.6/−23.6) ºC. During the V event, we record mean SSTs of 35.8 (+36.1/−35.4) ºC and SubT of 25.5 (+25.8/−25.4) ºC, reflecting a significant (*t*-test: $p < 0.001$) warming of 1.3–2.0°C (Figure 3b) compared to the pre-event interval. Temperatures drop after V to 34.5 (+35/−33.6) ºC (SubT = 24.5 (+24.9/−23.8) ºC), which is 0.2–0.7°C higher than before V (*t*-test: $p < 0.001$). The two previous TEX_{86}^{H}-based SST data points from Cramwinckel et al. (2018) for this interval at Site 959 are within the 95%CI's of background SSTs. Interestingly, the onset of warming leads the onset of the CIE by ~10 cm. In addition, the warming includes two warm phases with temperatures up to ~36°C, separated by a ~0.5°C cooling at the level where carbon isotope ratios reach minimum levels. Finally, throughout the studied interval, TEX_{86} shows a continuous ~50 cm variability, which is dampened during the hyperthermal.

3.4. Palynology

The palynological associations are mainly composed of dinocysts and remains of the organic inner-wall "linings" of benthic foraminifera (Figure 3c). The contribution of terrestrial elements (notably various types of pollen and spores) is generally low, with larger numbers, occasionally up to ~25% in certain samples. These intervals of higher proportions of terrestrial palynomorphs coincide with higher MS and Fe values, and darker sediment color. Unfortunately, the overall poor preservation of dinocysts prohibits the confident and complete quantification of the dinocyst assemblages for most analyzed samples; because of large number of unidentifiable (fragments of)

dinocysts, only 10 samples have more than 30 specimens that could be identified at family or genus level. Therefore, we discuss the dinocyst assemblages only in terms of broad qualitative and semi-quantitative results.

We do record the near-continuous occurrence of dinocysts that belong to the ecological groupings of *Areoligera*, *Spiniferites*, Protoperidinoids, Goniodomideae with an epicystal archeopyle (epicystal Goniodomids) and a rest group of Gonyaulacoids with a precingular archeopyle (cf. Frieling & Sluijs, 2018). In addition, many of the unidentified dinocysts represent skolochorate dinocysts probably of Gonyaulacoid affinity. The occurring Protoperidinoid cysts, notably *Selenopemphix* spp. and *Lejeunecysta* spp., represent obligate heterotrophic dinoflagellates today (e.g., Zonneveld et al., 2013). The identified epicystal Goniodomids, which in the modern ocean are typical of lagoonal, hypersaline settings (Zonneveld et al., 2013) are notably *Homotryblium* spp. and have been linked to strong stratification (and even harmful algal blooms in some cases) in the paleodomain (Brinkhuis, 1994; Cramwinckel et al., 2019; Pross & Schmiedl, 2002; Reichart et al., 2004). In effect, a major signal in the dinocysts assemblages is the sporadic dominance of *Homotryblium* spp., reaching above 90% of the identified component of the assemblages. In the middle part of the core, we record a few more numerous and/or prolonged occurrences of representatives of *Apectodinium*, *Areoligera*, Protoperidiniods and a single occurrence of a representative of *Senegalinum*.

4. Discussion

4.1. Magnitude of Carbon Isotope Excursion

The magnitude of the V-related CIE differs strongly between the bulk organic and carbonate records at Site 959 ($\Delta^{13}C_{carb}$ = 3.4‰, $\Delta^{13}C_{TOC}$ = 0.7‰). Importantly, the $\delta^{13}C_{carb}$ excursion is much larger than what is expected from the global exogenic signal, approximately ∼0.6‰ (Figure 4) (Lauretano et al., 2016; Sexton et al., 2011). We surmise that in the sedimentary environment of early Eocene Site 959, with relatively low biogenic $CaCO_3$ accumulation, authigenic carbonates, which are typically ^{13}C-depleted due to local organic carbon respiration (e.g., Botz et al., 1988), comprise a significant component of the bulk carbonate, similar to observations during earlier Eocene CIEs I1–L2 at Site 959 (Fokkema et al., 2024) and consistent with pore-water analysis (Mascle et al., 1996). Low $\delta^{13}C_{carb}$ values typically correspond with low $CaCO_3$wt% in lower Eocene deep ocean records (Kirtland Turner et al., 2014; Zachos et al., 2010). Consequently, this would exaggerate both background variability and the magnitude of the CIE in our record due to an increased fraction of authigenic carbonate in intervals with relatively low biogenic $CaCO_3$wt%.

4.2. Paleoenvironment and Water Column Structure

4.2.1. Background Climate State and Oceanography

The very low BIT index values (<0.01; Figure S2 in Supporting Information S1) and generally low numbers of terrestrial palynomorphs (mean = 4.8%) (Figure 3a) reflect an open marine early Eocene depositional setting at Site 959. Also the dinocyst assemblages are consistent with an open ocean setting with the continuous abundances of *Spiniferites* and particularly a few representatives of the open-ocean genus *Impagidinium* (Frieling & Sluijs, 2018). In contrast with these records, multiple samples are dominated by epicystal Goniodomid-cysts, specifically *Homotryblium* spp. (>75% of the relative dinocyst assemblage), traditionally interpreted to reflect lagoonal, hypersaline conditions (Brinkhuis, 1994; Pross & Schmiedl, 2002). However, dominances of such types of dinocysts have also been recorded under unequivocal open-ocean conditions, including the Eocene Site 959 (Cramwinckel et al., 2019; Fokkema et al., 2024; Frieling et al., 2018), attributed to so-called "hyper-stratified conditions"–potentially under high temperature (Cramwinckel et al., 2019), analogous to records from the "hyperstratified" episodes during the Pleistocene of the Arabian Sea (cf. Reichart et al., 2004), which enables a lifecycle without a sea floor interface. It is possible that the acmes we record here indeed reflect actual ancient dinoflagellate blooms, which is common in modern representatives of this group, for example, *Pyrodinium bahamense* and its cyst *Polysphaeridium zoharii* (Usup et al., 2012). In the paleo-domain, such a bloom-forming strategy of this group is supported by very high $\delta^{13}C$ values of *Eocladopyxis peniculata* cysts in an acme during the PETM on the New Jersey shelf (Sluijs et al., 2018). Hence, given the absence of evidence for large-scale transport of organic matter off the shelf, we suggest that the *Homotryblium* acmes/blooms at Site 959 occurred under warm and strongly stratified oceanic conditions. We postulate that the few intervals of relatively high contribution of terrestrial palynomorphs (Figure 3c) (partly) result from preservation bias, as terrestrial palynomorphs are more resistant to degradation than dinocysts.

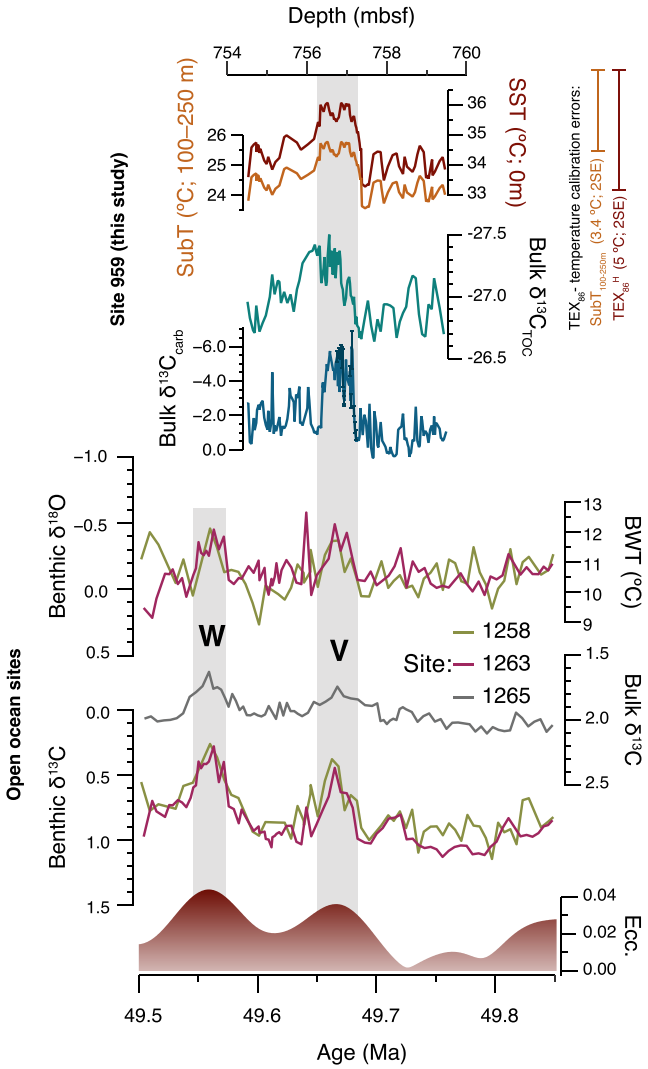

Figure 4. Representation of the V event at Site 959 and other Atlantic Ocean sites. Top: Site 959 data (against depth) with TEX_{86}-based SST and SubT, $\delta^{13}C_{TOC}$ and $\delta^{13}C_{carb}$. Calibration errors (2SE) of the used SST and SubT transfer functions are indicated on the top right. Bottom: benthic $\delta^{18}O$ from Site 1258 (Sexton et al., 2011) and Site 1263 (Lauretano et al., 2016, 2018) with $\delta^{18}O$-based bottom water temperatures on the right. Bulk $\delta^{13}C$ from Site 1265 (Westerhold et al., 2017), benthic $\delta^{13}C$ of Site 1258 and 1263 and orbital eccentricity (Laskar et al., 2011). Gray bands mark globally recognized CIEs V and W.

The consistent presence of protoperidinioid cysts, derived from heterotrophic dinoflagellates, implies sufficient food supply (Zonneveld et al., 2013). Moreover, sufficient organic material must have reached the ocean floor to sustain the relatively high TOCwt% and abundance of benthic foraminifera linings. The required high primary productivity presumably originated from regional wind-driven upwelling, inferred to occur at least since the middle Eocene based on organic geochemical data and palynological data (Cramwinckel et al., 2018; Wagner, 2002). Importantly, this productive setting around 49.7 Ma contrasts the records from ~54 to 52 Ma, where rich dinocyst assemblages lack protoperidinioids (Fokkema et al., 2024), suggesting that Eocene upwelling at Site 959 did not intensify until the end of the early Eocene (i.e., ~52–50 Ma). Neogene upwelling conditions at this site have previously been linked to the annual migration of the Atlantic Intertropical Convergence Zone (ITCZ) and the resulting West-African monsoonal response (Vallé et al., 2017; Wubben et al., 2024). Simulations suggest that West African monsoons should already have established during the Cretaceous and early Paleogene, and were relatively strong in this time interval compared to the Miocene due to the narrower Atlantic basin (Acosta et al., 2022). Based on the dominant factors enhancing the strength of monsoons, for example, geography and topography (Acosta et al., 2022), we infer that upwelling potentially started or intensified during the Eocene by progressive northward movement of the African plate, drifting Site 959 toward the equator.

4.2.2. Orbital Variability

The regular alternations observed in multiple proxy records (e.g., $CaCO_3$ content, MS, Fe, TOC%, total GDGT concentration), specifically on ~50-cm scale below the CIE (759.5–757.4 mbsf), suggests an orbital influence on the local oceanographic conditions and/or monsoon strength, analogous to that recorded in the Cretaceous (Beckmann et al., 2005) and Miocene (Wubben et al., 2024) at Site 959. As there is only one age-depth tiepoint in the studied core section, the responsible orbital cycle cannot be confidently identified. Although sedimentation rates of the studied section are uncertain, the long-term background sedimentation rates of 0.8–1.4 cm/kyr (Fokkema et al., 2024) imply that the persistent 50-cm variability would approximate the 41-kyr obliquity band. However, obliquity has neglectable direct influence on equatorial insolation, whereas variability in the strength of the monsoons is usually associated with Earth's ~20-kyr precession cycles, and only obliquity when remotely forced (e.g., Tuenter et al., 2003). On the other hand, dominant obliquity forcing has been observed in low latitudes (Weedon et al., 1997) and exerts influence on Neogene Mediterranean sapropel occurrences and monsoon dynamics (e.g., Bosmans et al., 2015; Lourens et al., 1996). In addition, obliquity is also possibly more pronounced under very low orbital eccentricity configurations (Westerhold et al., 2014), as also recorded in the early Miocene at Site 959 (Wubben et al., 2023). Indeed, a ~2.4-Myr orbital-eccentricity minimum just precedes the V event (Laskar et al., 2011; Lauretano et al., 2018) (Figure 4), supporting the possibility of obliquity forcing on monsoonal strength prior to V. Nevertheless, without additional age control, there remains a possibility that the cyclic variations prior to V represent precession.

The cycles below the V event coincide with temperature variability of ~0.8–1°C. This variability is mirrored in $\delta^{13}C_{TOC}$, with minimum TEX_{86} values coinciding with $\delta^{13}C_{TOC}$ minima, which suggests that during enhanced upwelling of ^{13}C depleted subsurface waters, the shallow waters cooled and vice versa (Figure 3). No clear cyclic patterns are present in the interval above V. Importantly, the absence of the W CIE, which occurred ~100 kyr after V, implies at least a doubling of sedimentation rate if the pre-event variations represent obliquity. Accordingly, a relative increase in, $CaCO_3$, Si and TOCwt% (Figure 3a) suggest higher productivity and biogenic sediment

accumulation rates compared to the lower interval, potentially facilitating the required increase if the supply of siliciclastic materials remained constant.

4.2.3. Environmental Change During Hyperthermal V

The maximum TEX_{86} values recorded during the V event, translating to TEX_{86}^{H}-based SSTs of 36.1°C, are close to that recorded during hyperthermals I1–L2 (maximum SSTs of 36–36.4°C; Figure 2) by Fokkema et al. (2024). The magnitude of warming (ΔT = 1.3–2.0°C) is, however, slightly higher than the magnitude warming that was recorded during the preceding early Eocene hyperthermals at Site 959 (averaged ∼0.7–1°C; Fokkema et al., 2024). Peak warmth during hyperthermal V manifests in two peaks (757.0 and 756.5 mbsf) separated by a plateau. We surmise that this reflects a continuation of the pre-event orbitally forced variability in monsoon strength. Accordingly, the two temperature peaks are marked by relatively high $\delta^{13}C_{TOC}$ values, suggesting they represent periods of minimal upwelling, similar to the intervals of higher $\delta^{13}C_{TOC}$ and SST surrounding the event.

In addition to warming, the V event is characterized by increased TOCwt%, Fe, MS and a decline in the $CaCO_3$ wt% and Si in the sediment. Frieling et al. (2018) discussed multiple mechanisms that might have induced low $CaCO_3$wt% contents in PETM records at Site 959. Ocean acidification may well have impacted carbonate preservation, but this may have been limited, due to the relatively shallow paleodepth (∼1,000 m) of Site 959 during the early Eocene (Frieling et al., 2018). However, similar to the PETM interpretation by Frieling et al. (2018), we infer that the low $CaCO_3$wt% during the CIE can be attributed to remineralization of organic material in the sediment and possibly also to attenuation of biogenic $CaCO_3$ formation–potentially by heat stress (Aze et al., 2014; Frieling et al., 2018). As we observed no large-scale increases in productivity-associated dinocysts during the V event, the TOC% increase presumably resulted from increased organic matter preservation, combined with reduced $CaCO_3$ and Si content.

Although — as discussed above — dinocyst preservation is poor in general, we do record a subtle dinocyst response during hyperthermal V. Notably, few occurrences of the thermophilic dinocyst taxon *Apectodinium* are recorded during the hyperthermal (Figure 3c). Representatives of this genus are known to occur in high numbers surrounding the PETM interval at Site 959 (Frieling et al., 2018) (and globally during the PETM, e.g., Crouch et al., 2001; Denison, 2021). Presumably other factors than solely temperature allowed for the occurrence of *Apectodinium* spp. to Site 959; perhaps the supply of nutrients. Another feature is abundant *Areoligera* spp. at 756.8 mbsf. This peak coincides with the highest relative abundance of dinocysts (>75%), and elevated TOCwt% (Figure 2). Although perhaps masked by poor preservation, the epicystal Goniodomid-cysts do not seem to significantly increase during the event, conflicting with the occurrence of (thermal) hyperstratification during the peak MECO (Cramwinckel et al., 2019).

4.3. Polar Amplification of Climate Change

Previous work has compared the warming of early Eocene hyperthermals in the tropics to that of higher latitudes to assess ice-free polar amplification of climate change, finding a relative consistent amplification factor of approximately ∼2 (Fokkema et al., 2024; Frieling et al., 2017; Tierney et al., 2022). The only temperature and ecological records from the high latitudes that cover internal climate variability in the EECO (i.e., IODP Site 1356, Wilkes Land) are still not fully resolved on eccentricity timescales (Bijl et al., 2013; Pross et al., 2012). Therefore, to assess potential extratropical amplification of warming during hyperthermal V, we compare the warming at Site 959 with that in the deep ocean benthic foraminiferal $\delta^{18}O$-based bottom water temperature (BWT) records, following the approach of Cramwinckel et al. (2018) and Fokkema et al. (2024). A caveat of utilizing $\delta^{18}O$-based BWTs is their mismatch with clumped isotope-based BWT records (Meckler et al., 2022), suggestive of divergent regional $\delta^{18}O$ signals. Yet, there are no significant mismatches reported between benthic $\delta^{18}O$- and clumped isotope-based reconstructions of hyperthermal-scale temperature variability during the early Eocene (Agterhuis et al., 2022). Importantly, the $\delta^{18}O$-based BWTs match the pollen-derived coldest month temperatures at Wilkes Land (Pross et al., 2012), in line with the notion that early Eocene bottom water formation occurred dominantly in the Southern Ocean close to the Antarctic margin (Hollis et al., 2012; Zhang et al., 2022). For comparison with deep-ocean BWT variability, we transferred published $\delta^{18}O$ data from Site 1258 (Sexton et al., 2011) and Site 1263 (Lauretano et al., 2016, 2018) to temperature by the equation by Kim and O'Neil (1997), modified by Bemis et al. (1998), and using a seawater $\delta^{18}O$ of −1‰ VPDB, following the

procedure as recommended by Hollis et al. (2019). An analytical uncertainty in ΔBWT of 0.4°C was used (Lauretano et al., 2018).

In the deep ocean benthic foraminifera isotope records, hyperthermal V was marked by an averaged 0.44‰ $\delta^{18}O$ excursion, consistent with a warming of 2.0(±0.4) ºC (Lauretano et al., 2018) (Figure 4). When compared to the tropical surface warming of 1.3–2.0 during V at Site 959, this implies an absent or small amplification factor between the tropics and the polar region of deep-water formation (0.8–1.8), which mismatches the polar amplification recorded during multiple early EECO hyperthermals (1.8–2.4) (Fokkema et al., 2024) and during the PETM ~1.6–2.7 (Frieling et al., 2017; Tierney et al., 2022) (Figure S3 in Supporting Information S1). We surmise that a locally biased SST signal at Site 959, presumably through decrease in upwelling intensity during the V event, led to reduced polar amplification estimates.

4.4. Prolonged Organic Carbon Isotope Excursion

The recovery of the CIEs in the $\delta^{13}C_{TOC}$ and $\delta^{13}C_{carb}$ are significantly offset; $\delta^{13}C_{TOC}$ lags $\delta^{13}C_{carb}$ by 55 cm, which represents ~40–70 kyr, following long-term background sedimentation rates of 0.8–1.4 cm/kyr (calculated between Top *Tribarchaitus orthostylus* (Core 36R) and Top *Discoaster lodoensis* (Core 39R–Core 38R); Figure 2). This is inconsistent with the premise that carbon utilized in photosynthesis and calcification are both fixed from the same dissolved inorganic carbon (DIC) pool. This observation suggests that the recovery of the CIE in the $\delta^{13}C_{carb}$ record is obscured by diagenetic processes, or that an organic matter component with low $\delta^{13}C$ values contributes to sedimentary $\delta^{13}C_{TOC}$ values in the direct aftermath of the CIE. Notably, TEX_{86}, amongst other proxy records (e.g., Ca/Si, $CaCO_3$wt%, Si/Fe, TOC%) returns back to approximately pre-event values just above the ending of the $\delta^{13}C_{carb}$ CIE at 756.3 mbsf, suggesting that this depth represents the end of hyperthermal V, and that the $\delta^{13}C_{TOC}$ lags behind the other records.

Potentially, the longer tail in the $\delta^{13}C_{TOC}$ record represents terrestrial organic carbon produced during the CIE, transported to the marine realm after the event. However, this is inconsistent with the relatively short (~5 kyr) time between the production of terrestrial organic matter and its transport to the ocean (Cole and Caraco, 2001) and the consistently low relative amounts of terrestrial organic matter in our materials.

In the modern ocean, the oldest (most ^{14}C-depleted) phase of carbon resides as (refractory) dissolved organic carbon (DOC_{ref}) in the Pacific Ocean at 2 km water depth, with an estimated age of 12 kyrs (Follett et al., 2014). Potentially, the long bulk $\delta^{13}C_{TOC}$ tail thus reflects contributions from this older DOC_{ref} pool in the aftermath of V. This chemically inert phase of DOC is likely generated by the microbial carbon pump (Jiao et al., 2010). The bioavailability of DOC_{ref} increases by upwelling (Fang et al., 2020), which allows for a biotic conversion of ^{13}C-depleted DOC_{ref} to ^{13}C-depleted POC (Shen & Benner, 2018). Specifically, DOC_{ref} is suggested to physically disintegrate by radiation at the surface ocean and biologically degrade by the addition of more readily degradable organic matter (Fang et al., 2020; Shen & Benner, 2018). Furthermore, based on the presence of sponge spicules in younger intervals at Site 959 (Mascle et al., 1996), while they would not be well preserved in the Eocene porcellanites, this site might facilitate the DOC to POC conversion by benthic filter feeding sponges. We surmise that Site 959 holds the potential to transform $\delta^{13}C$ depleted DOC_{ref} to POC, either at the surface and/or the deep ocean, which will eventually leave an imprint in the sediment record as a prolonged $\delta^{13}C_{TOC}$ tail.

5. Conclusions

Tropical warming and biotic change accompanied a significant CIE during the end of the EECO in the tropical Atlantic at Site 959. The CIE is identified as the "V" event at 49.7 Ma, by combining published biostratigraphic constraints and new carbon isotope stratigraphy. TEX_{86} paleothermometry indicates a temperature increase of 1.3–2.0°C relative to pre-event values, confirming that this event represents a transient global warming event, or hyperthermal. Recorded peak SSTs during V are within the range of that of earlier hyperthermals during the EECO. Interestingly, the recovery of the CIE in $\delta^{13}C_{TOC}$ is delayed relative to that in $\delta^{13}C_{carb}$. We postulate that upwelling of old and deep (^{13}C-depleted) DOC_{ref} contributed to the long bulk $\delta^{13}C_{TOC}$ tail.

The recorded background paleoceanography during this time differs from earlier Eocene records from the same site: wind-driven upwelling facilitated a more productive depositional setting reflected in relatively organic rich sediments and presence of heterotrophic dinoflagellate cyst remains. Variations in upwelling intensity, presumably orbitally driven via monsoons, are reflected in multiple proxy indicators: notably affecting carbon

isotopes and temperatures in the (shallow sub-) surface ocean. In strong contrast to the recorded upwelling is the sporadic dinocyst dominance by hyper-stratification-related genera, which seems a common feature in Eocene Site 959 records (Cramwinckel et al., 2019; Fokkema et al., 2024; Frieling et al., 2018).

Conflict of Interest

One of the co-authors is a member of the editorial board of Paleoceanography and Paleoclimatology.

Data Availability Statement

All new data presented in this work are available on Zenodo (Sluijs et al., 2024).

Acknowledgments
This project used samples retrieved and curated by the IODP and predecessors. We thank Antoinette van den Dikkenberg, Natasja Welters, Giovanni Dammers, Desmond Eefting, Maxim Krasnoperov and Arnold van Dijk for their assistance in the lab and technical support. This research was funded by European Research Council Grant 771497 awarded to A.S. under the H2020 program, by the Deutsche Forschungsgemeinschaft (DFG, German Research Foundation) to U.R. and T.W. (project nos. 28504316 and 320221997) and under Germany's Excellence Strategy–EXC-2077–390741603. C.A. was funded by the RETURN Extended Partnership from the European Union Next-GenerationEU (National Recovery and Resilience Plan–NRRP, Mission 4, Component 2, Investment 1.3–D.D. 1243 2/8/2022, PE0000005. We thank two anonymous reviewers for their constructive comments and Matthew Huber for editorial handling.

References

Acosta, R. P., Ladant, J., Zhu, J., & Poulsen, C. J. (2022). Evolution of the Atlantic intertropical convergence zone, and the south American and African monsoons over the past 95-Myr and their impact on the tropical rainforests. *Paleoceanography and Paleoclimatology*, *37*(7), e2021PA004383. https://doi.org/10.1029/2021PA004383

Agnini, C., Fornaciari, E., Raffi, I., Catanzariti, R., Pälike, H., Backman, J., & Rio, D. (2014). Biozonation and biochronology of Paleogene calcareous nannofossils from low and middle latitudes. *Newsletters on Stratigraphy*, *47*(2), 131–181. https://doi.org/10.1127/0078-0421/2014/0042

Agnini, C., Macrì, P., Backman, J., Brinkhuis, H., Fornaciari, E., Giusberti, L., et al. (2009). An early Eocene carbon cycle perturbation at ~52.5 Ma in the Southern Alps: Chronology and biotic response. *Paleoceanography*, *24*(2), PA2209. https://doi.org/10.1029/2008PA001649

Agnini, C., Muttoni, G., Kent, D. V., & Rio, D. (2006). Eocene biostratigraphy and magnetic stratigraphy from Possagno, Italy: The calcareous nannofossil response to climate variability. *Earth and Planetary Science Letters*, *241*(3–4), 815–830. https://doi.org/10.1016/j.epsl.2005.11.005

Agterhuis, T., Ziegler, M., de Winter, N. J., & Lourens, L. J. (2022). Warm deep-sea temperatures across Eocene Thermal Maximum 2 from clumped isotope thermometry. *Communications Earth & Environment*, *3*(1), 39. https://doi.org/10.1038/s43247-022-00350-8

Anagnostou, E., John, E. H., Babila, T. L., Sexton, P. F., Ridgwell, A., Lunt, D. J., et al. (2020). Proxy evidence for state-dependence of climate sensitivity in the Eocene greenhouse. *Nature Communications*, *11*(1), 4436. https://doi.org/10.1038/s41467-020-17887-x

Aze, T., Pearson, P. N., Dickson, A. J., Badger, M. P. S., Bown, P. R., Pancost, R. D., et al. (2014). Extreme warming of tropical waters during the Paleocene–Eocene thermal maximum. *Geology*, *42*(9), 739–742. https://doi.org/10.1130/G35637.1

Backman, J. (1986). Late Paleocene to middle Eocene calcareous nannofossil biochronology from the Shatsky rise, Walvis Ridge and Italy. *Palaeogeography, Palaeoclimatology, Palaeoecology*, *57*(1), 43–59. https://doi.org/10.1016/0031-0182(86)90005-2

Beckmann, B., Flögel, S., Hofmann, P., Schulz, M., & Wagner, T. (2005). Orbital forcing of Cretaceous river discharge in tropical Africa and ocean response. *Nature*, *437*(7056), 241–244. https://doi.org/10.1038/nature03976

Bemis, B. E., Spero, H. J., Bijma, J., & Lea, D. W. (1998). Reevaluation of the oxygen isotopic composition of planktonic foraminifera: Experimental results and revised paleotemperature equations. *Paleoceanography*, *13*(2), 150–160. https://doi.org/10.1029/98PA00070

Berndt, C., Planke, S., Alvarez Zarikian, C. A., Frieling, J., Jones, M. T., Millett, J. M., et al. (2023). Shallow-water hydrothermal venting linked to the Palaeocene–Eocene thermal maximum. *Nature Geoscience*, *16*(9), 803–809. https://doi.org/10.1038/s41561-023-01246-8

Bijl, P. K., Bendle, J. A. P., Bohaty, S. M., Pross, J., Schouten, S., Tauxe, L., et al. (2013). Eocene cooling linked to early flow across the Tasmanian Gateway. *Proceedings of the National Academy of Sciences*, *110*(24), 9645–9650. https://doi.org/10.1073/pnas.1220872110

Bijl, P. K., Frieling, J., Cramwinckel, M. J., Boschman, C., Sluijs, A., & Peterse, F. (2021). Maastrichtian–Rupelian paleoclimates in the southwest Pacific – A critical re-evaluation of biomarker paleothermometry and dinoflagellate cyst paleoecology at Ocean Drilling program site 1172. *Climate of the Past*, *17*(6), 2393–2425. https://doi.org/10.5194/cp-17-2393-2021

Bijl, P. K., Schouten, S., Sluijs, A., Reichart, G.-J., Zachos, J. C., & Brinkhuis, H. (2009). Early Palaeogene temperature evolution of the southwest Pacific Ocean. *Nature*, *461*(7265), 776–779. https://doi.org/10.1038/nature08399

Bosmans, J. H. C., Drijfhout, S. S., Tuenter, E., Hilgen, F. J., & Lourens, L. J. (2015). Response of the North African summer monsoon to precession and obliquity forcing's in the EC-Earth GCM. *Climate Dynamics*, *44*(1–2), 279–297. https://doi.org/10.1007/s00382-014-2260-z

Botz, R., Faber, E., Whiticar, M. J., & Brooks, J. M. (1988). Authigenic carbonates in sediments from the Gulf of Mexico. *Earth and Planetary Science Letters*, *88*(3–4), 263–272. https://doi.org/10.1016/0012-821X(88)90083-0

Brinkhuis, H. (1994). Late Eocene to early Oligocene dinoflagellate cysts from the Priabonian type-area (Northeast Italy): Biostratigraphy and paleoenvironmental interpretation. *Palaeogeography, Palaeoclimatology, Palaeoecology*, *107*(1–2), 121–163. https://doi.org/10.1016/0031-0182(94)90168-6

Cappelli, C., Bown, P. R., Westerhold, T., Bohaty, S. M., Riu, M., Lobba, V., et al. (2019). The early to middle Eocene transition: An integrated calcareous nannofossil and stable isotope record from the northwest Atlantic Ocean (integrated Ocean Drilling program site U1410). *Paleoceanography and Paleoclimatology*, *34*(12), 1913–1930. https://doi.org/10.1029/2019PA003686

Cole, J. J., Caraco, N. F., & Caraco, N. F. (2001). Carbon in catchments: Connecting terrestrial carbon losses with aquatic metabolism. *Marine and Freshwater Research*, *52*(1), 101. https://doi.org/10.1071/MF00084

Cramer, B. S., Wright, J. D., Kent, D. V., & Aubry, M.-P. (2003). Orbital climate forcing of D13C excursions in the late Paleocene—early Eocene (chrons C24n–C25n). *Paleoceanography*, *18*(4), 1097. https://doi.org/10.1029/2003PA000909

Cramwinckel, M. J., Huber, M., Kocken, I. J., Agnini, C., Bijl, P. K., Bohaty, S. M., et al. (2018). Synchronous tropical and polar temperature evolution in the Eocene. *Nature*, *559*(7714), 382–386. https://doi.org/10.1038/s41586-018-0272-2

Cramwinckel, M. J., van der Ploeg, R., Bijl, P. K., Peterse, F., Bohaty, S. M., Röhl, U., et al. (2019). Harmful algae and export production collapse in the equatorial Atlantic during the zenith of Middle Eocene Climatic Optimum warmth. *Geology*, *47*(3), 247–250. https://doi.org/10.1130/G45614.1

Crouch, E. M., Heilmann-Clausen, C., Brinkhuis, H., Morgans, H. E. G., Rogers, K. M., Egger, H., & Schmitz, B. (2001). Global dinoflagellate event associated with the late Paleocene thermal maximum. *Geology*, *29*(4), 315. https://doi.org/10.1130/0091-7613(2001)029<0315:GDEAWT>2.0.CO;2

DeConto, R. M., Galeotti, S., Pagani, M., Tracy, D., Schaefer, K., Zhang, T., et al. (2012). Past extreme warming events linked to massive carbon release from thawing permafrost. *Nature*, *484*(7392), 87–91. https://doi.org/10.1038/nature10929

Denison, C. N. (2021). Stratigraphic and sedimentological aspects of the worldwide distribution of Apectodinium in Paleocene/Eocene Thermal Maximum deposits. *Geological Society, London, Special Publications Home*, *511*(1), 269–308. https://doi.org/10.1144/SP511-2020-46

Dickens, G. R., Castillo, M. M., & Walker, J. C. G. (1997). A blast of gas in the latest Paleocene: Simulating first-order effects of massive dissociation of oceanic methane hydrate. *Geology*, *25*(3), 259. https://doi.org/10.1130/0091-7613(1997)025<0259:ABOGIT>2.3.CO;2

Dickens, G. R., O'Neil, J. R., Rea, D. K., & Owen, R. M. (1995). Dissociation of oceanic methane hydrate as a cause of the carbon isotope excursion at the end of the Paleocene. *Paleoceanography*, *10*(6), 965–971. https://doi.org/10.1029/95PA02087

Dunkley Jones, T., Lunt, D. J., Schmidt, D. N., Ridgwell, A., Sluijs, A., Valdes, P. J., & Maslin, M. (2013). Climate model and proxy data constraints on ocean warming across the Paleocene–Eocene Thermal Maximum. *Earth-Science Reviews*, *125*, 123–145. https://doi.org/10.1016/j.earscirev.2013.07.004

Fang, L., Lee, S., Lee, S.-A., Hahm, D., Kim, G., Druffel, E. R. M., & Hwang, J. (2020). Removal of refractory dissolved organic carbon in the Amundsen sea, Antarctica. *Scientific Reports*, *10*(1), 1213. https://doi.org/10.1038/s41598-020-57870-6

Fokkema, C. D., Agterhuis, T., Gerritsma, D., De Goeij, M., Liu, X., De Regt, P., et al. (2024). Polar amplification of orbital-scale climate variability in the early Eocene greenhouse world. *Climate of the Past*, *20*(6), 1303–1325. https://doi.org/10.5194/cp-20-1303-2024

Fokkema, C. D., Buijs, S., Bialik, O. M., Meilijson, A., Waldmann, N. D., Makovsky, Y., et al. (2022). Late Paleocene to middle Eocene carbon isotope stratigraphy of the northern Negev, Southern Israel: Potential for paleoclimate reconstructions. *Newsletters on Stratigraphy*, *55*(3), 361–384. https://doi.org/10.1127/nos/2022/0684

Follett, C. L., Repeta, D. J., Rothman, D. H., Xu, L., & Santinelli, C. (2014). Hidden cycle of dissolved organic carbon in the deep ocean. *Proceedings of the National Academy of Sciences*, *111*(47), 16706–16711. https://doi.org/10.1073/pnas.1407445111

Frieling, J., Gebhardt, H., Huber, M., Adekeye, O. A., Akande, S. O., Reichart, G.-J., et al. (2017). Extreme warmth and heat-stressed plankton in the tropics during the Paleocene-Eocene Thermal Maximum. *Science Advances*, *3*(3), e1600891. https://doi.org/10.1126/sciadv.1600891

Frieling, J., Peterse, F., Lunt, D. J., Bohaty, S. M., Sinninghe Damsté, J. S., Reichart, G.-J., & Sluijs, A. (2019). Widespread warming before and elevated barium burial during the Paleocene-Eocene thermal maximum: Evidence for methane hydrate release? *Paleoceanography and Paleoclimatology*, *34*(4), 546–566. https://doi.org/10.1029/2018PA003425

Frieling, J., Reichart, G. J., Middelburg, J. J., Rohl, U., Westerhold, T., Bohaty, S. M., & Sluijs, A. (2018). Tropical Atlantic climate and ecosystem regime shifts during the Paleocene–Eocene thermal maximum. *Climate of the Past*, *14*(1), 39–55. https://doi.org/10.5194/cp-14-39-2018

Frieling, J., & Sluijs, A. (2018). Towards quantitative environmental reconstructions from ancient non-analogue microfossil assemblages: Ecological preferences of Paleocene – Eocene dinoflagellates. *Earth-Science Reviews*, *185*, 956–973. https://doi.org/10.1016/j.earscirev.2018.08.014

Galeotti, S., Krishnan, S., Pagani, M., Lanci, L., Gaudio, A., Zachos, J. C., et al. (2010). Orbital chronology of early Eocene hyperthermals from the Contessa Road Section, central Italy. *Earth and Planetary Science Letters*, *290*(1–2), 192–200. https://doi.org/10.1016/j.epsl.2009.12.021

Gaskell, D. E., Huber, M., O'Brien, C. L., Inglis, G. N., Acosta, R. P., Poulsen, C. J., & Hull, P. M. (2022). The latitudinal temperature gradient and its climate dependence as inferred from foraminiferal δ 18 O over the past 95 million years. *Proceedings of the National Academy of Sciences*, *119*(11), e2111332119. https://doi.org/10.1073/pnas.2111332119

Gibbs, S. J., Bown, P. R., Murphy, B. H., Sluijs, A., Edgar, K. M., Pälike, H., et al. (2012). Scaled biotic disruption during early Eocene global warming events. *Biogeosciences*, *9*(11), 4679–4688. https://doi.org/10.5194/bg-9-4679-2012

Ho, S. L., & Laepple, T. (2016). Flat meridional temperature gradient in the early Eocene in the subsurface rather than surface ocean. *Nature Geoscience*, *9*(8), 606–610. https://doi.org/10.1038/ngeo2763

Hollis, C. J., Dunkley Jones, T., Anagnostou, E., Bijl, P. K., Cramwinckel, M. J., Cui, Y., et al. (2019). The DeepMIP contribution to PMIP4: Methodologies for selection, compilation and analysis of latest Paleocene and early Eocene climate proxy data, incorporating version 0.1 of the DeepMIP database. *Geoscientific Model Development*, *12*(7), 3149–3206. https://doi.org/10.5194/gmd-12-3149-2019

Hollis, C. J., Taylor, K. W. R., Handley, L., Pancost, R. D., Huber, M., Creech, J. B., et al. (2012). Early Paleogene temperature history of the southwest Pacific Ocean: Reconciling proxies and models. *Earth and Planetary Science Letters*, *349–350*, 53–66. https://doi.org/10.1016/j.epsl.2012.06.024

Hopmans, E. C., Schouten, S., & Sinninghe Damsté, J. S. (2016). The effect of improved chromatography on GDGT-based palaeoproxies. *Organic Geochemistry*, *93*, 1–6. https://doi.org/10.1016/j.orggeochem.2015.12.006

Hopmans, E. C., Weijers, J. W. H., Schefuß, E., Herfort, L., Sinninghe Damsté, J. S., & Schouten, S. (2004). A novel proxy for terrestrial organic matter in sediments based on branched and isoprenoid tetraether lipids. *Earth and Planetary Science Letters*, *224*(1–2), 107–116. https://doi.org/10.1016/j.epsl.2004.05.012

Hupp, B. N., Kelly, D. C., & Williams, J. W. (2022). Isotopic filtering reveals high sensitivity of Planktic calcifiers to Paleocene–Eocene thermal maximum warming and acidification. *Proceedings of the National Academy of Sciences*, *119*(9), e2115561119. https://doi.org/10.1073/pnas.2115561119

Hurley, S. J., Lipp, J. S., Close, H. G., Hinrichs, K.-U., & Pearson, A. (2018). Distribution and export of isoprenoid tetraether lipids in suspended particulate matter from the water column of the Western Atlantic Ocean. *Organic Geochemistry*, *116*, 90–102. https://doi.org/10.1016/j.orggeochem.2017.11.010

Inglis, G. N., Bragg, F., Burls, N. J., Cramwinckel, M. J., Evans, D., Foster, G. L., et al. (2020). Global mean surface temperature and climate sensitivity of the early Eocene climatic Optimum (EECO), Paleocene–Eocene thermal maximum (PETM), and latest Paleocene. *Climate of the Past*, *16*(5), 1953–1968. https://doi.org/10.5194/cp-16-1953-2020

Jiao, N., Herndl, G. J., Hansell, D. A., Benner, R., Kattner, G., Wilhelm, S. W., et al. (2010). Microbial production of recalcitrant dissolved organic matter: Long-term carbon storage in the global ocean. *Nature Reviews Microbiology*, *8*(8), 593–599. https://doi.org/10.1038/nrmicro2386

Kennett, J. P., & Stott, L. D. (1991). Abrupt deep-sea warming, palaeoceanographic changes and benthic extinctions at the end of the Palaeocene. *Nature*, *353*(6341), 225–229. https://doi.org/10.1038/353225a0

Kim, J.-H., van der Meer, J., Schouten, S., Helmke, P., Willmott, V., Sangiorgi, F., et al. (2010). New indices and calibrations derived from the distribution of crenarchaeal isoprenoid tetraether lipids: Implications for past sea surface temperature reconstructions. *Geochimica et Cosmochimica Acta*, *74*(16), 4639–4654. https://doi.org/10.1016/j.gca.2010.05.027

Kim, S.-T., & O'Neil, J. R. (1997). Equilibrium and nonequilibrium oxygen isotope effects in synthetic carbonates. *Geochimica et Cosmochimica Acta*, *61*(16), 3461–3475. https://doi.org/10.1016/S0016-7037(97)00169-5

Kirtland Turner, S., Sexton, P. F., Charles, C. D., & Norris, R. D. (2014). Persistence of carbon release events through the peak of early Eocene global warmth. *Nature Geoscience*, *7*(10), 748–751. https://doi.org/10.1038/ngeo2240

Kocken, I. J. (2023). Colourlog: Generate plots of colourlogs from core photographs (v0.0.4) [Software]. *Zenodo*. https://doi.org/10.5281/zenodo.7869340

Kurtz, A. C., Kump, L. R., Arthur, M. A., Zachos, J. C., & Paytan, A. (2003). Early Cenozoic decoupling of the global carbon and sulfur cycles. *Paleoceanography*, *18*(4), 1090. https://doi.org/10.1029/2003PA000908

Laskar, J., Fienga, A., Gastineau, M., & Manche, H. (2011). La2010: A new orbital solution for the long-term motion of the Earth. *Astronomy and Astrophysics*, *532*, A89. https://doi.org/10.1051/0004-6361/201116836

Lauretano, V., Hilgen, F. J., Zachos, J. C., & Lourens, L. J. (2016). Astronomically tuned age model for the early Eocene carbon isotope events: A new high-resolution δ13 Cbenthic record of ODP site 1263 between ~ 49 and ~ 54 Ma. *Newsletters on Stratigraphy*, *49*(2), 383–400. https://doi.org/10.1127/nos/2016/0077

Lauretano, V., Zachos, J. C., & Lourens, L. J. (2018). Orbitally paced carbon and deep-sea temperature changes at the peak of the early Eocene climatic Optimum. *Paleoceanography and Paleoclimatology*, *33*(10), 1050–1065. https://doi.org/10.1029/2018PA003422

Laurin, J., Meyers, S. R., Galeotti, S., & Lanci, L. (2016). Frequency modulation reveals the phasing of orbital eccentricity during Cretaceous Oceanic Anoxic Event II and the Eocene hyperthermals. *Earth and Planetary Science Letters*, *442*, 143–156. https://doi.org/10.1016/j.epsl.2016.02.047

Littler, K., Röhl, U., Westerhold, T., & Zachos, J. C. (2014). A high-resolution benthic stable-isotope record for the South Atlantic: Implications for orbital-scale changes in Late Paleocene–Early Eocene climate and carbon cycling. *Earth and Planetary Science Letters*, *401*, 18–30. https://doi.org/10.1016/j.epsl.2014.05.054

Lourens, L. J., Antonarakou, A., Hilgen, F. J., Van Hoof, A. A. M., Vergnaud-Grazzini, C., & Zachariasse, W. J. (1996). Evaluation of the Plio-Pleistocene astronomical timescale. *Paleoceanography*, *11*(4), 391–413. https://doi.org/10.1029/96PA01125

Lourens, L. J., Sluijs, A., Kroon, D., Zachos, J. C., Thomas, E., Röhl, U., et al. (2005). Astronomical pacing of late Palaeocene to early Eocene global warming events. *Nature*, *435*(7045), 1083–1087. https://doi.org/10.1038/nature03814

Mascle, J., Lohmann, G. P., Clift, P. D., & Scientific Party (Eds.). (1996). *Proceedings of the Ocean Drilling Program, 159* (Vol. 159). Ocean Drilling Program. https://doi.org/10.2973/odp.proc.ir.159.1996

Massana, R., DeLong, E. F., & Pedrós-Alió, C. (2000). A few Cosmopolitan Phylotypes dominate planktonic archaeal assemblages in widely different oceanic provinces. *Applied and Environmental Microbiology*, *66*(5), 1777–1787. https://doi.org/10.1128/AEM.66.5.1777-1787.2000

McInerney, F. A., & Wing, S. L. (2011). The Paleocene-Eocene thermal maximum: A perturbation of carbon cycle, climate, and biosphere with implications for the future. *Annual Review of Earth and Planetary Sciences*, *39*(1), 489–516. https://doi.org/10.1146/annurev-earth-040610-133431

Meckler, A. N., Sexton, P. F., Piasecki, A. M., Leutert, T. J., Marquardt, J., Ziegler, M., et al. (2022). Cenozoic evolution of deep ocean temperature from clumped isotope thermometry. *Science*, *377*(6601), 86–90. https://doi.org/10.1126/science.abk0604

Piedrahita, V. A., Galeotti, S., Zhao, X., Roberts, A. P., Rohling, E. J., Heslop, D., et al. (2022). Orbital phasing of the Paleocene-Eocene thermal maximum. *Earth and Planetary Science Letters*, *598*, 117839. https://doi.org/10.1016/j.epsl.2022.117839

Pross, J., & Brinkhuis, H. (2005). Organic-walled dinoflagellate cysts as paleoenvironmental indicators in the Paleogene; a synopsis of concepts. *Paläontologische Zeitschrift*, *79*(1), 53–59. https://doi.org/10.1007/BF03021753

Pross, J., Contreras, L., Bijl, P. K., Greenwood, D. R., Bohaty, S. M., Schouten, S., et al. (2012). Persistent near-tropical warmth on the Antarctic continent during the early Eocene epoch. *Nature*, *488*(7409), 73–77. https://doi.org/10.1038/nature11300

Pross, J., & Schmiedl, G. (2002). Early Oligocene dinoflagellate cysts from the upper Rhine Graben (SW Germany): Paleoenvironmental and paleoclimatic implications. *Marine Micropaleontology*, *45*, 1–24. https://doi.org/10.1016/s0377-8398(01)00046-9

Rattanasriampaipong, R., Zhang, Y. G., Pearson, A., Hedlund, B. P., & Zhang, S. (2022). Archaeal lipids trace ecology and evolution of marine ammonia-oxidizing archaea. *Proceedings of the National Academy of Sciences*, *119*(31), e2123193119. https://doi.org/10.1073/pnas.2123193119

Reichart, G.-J., Brinkhuis, H., Huiskamp, F., & Zachariasse, W. J. (2004). Hyperstratification following glacial overturning events in the northern Arabian Sea. *Paleoceanography*, *19*(2). https://doi.org/10.1029/2003PA000900

Rush, W. D., Self-Trail, J., Zhang, Y., Sluijs, A., Brinkhuis, H., Zachos, J., et al. (2023). Assessing environmental change associated with early Eocene hyperthermals in the Atlantic Coastal Plain, USA. *Climate of the Past*, *19*(8), 1677–1698. https://doi.org/10.5194/cp-19-1677-2023

Schrag, D. P., DePaolo, D. J., & Richter, F. M. (1995). Reconstructing past sea surface temperatures: Correcting for diagenesis of bulk marine carbonate. *Geochimica et Cosmochimica Acta*, *59*(11), 2265–2278. https://doi.org/10.1016/0016-7037(95)00105-9

Setty, S., Cramwinckel, M. J., Van Nes, E. H., Van De Leemput, I. A., Dijkstra, H. A., Lourens, L. J., et al. (2023). Loss of Earth system resilience during early Eocene transient global warming events. *Science Advances*, *9*(14), eade5466. https://doi.org/10.1126/sciadv.ade5466

Sexton, P. F., Norris, R. D., Wilson, P. A., Pälike, H., Westerhold, T., Röhl, U., et al. (2011). Eocene global warming events driven by ventilation of oceanic dissolved organic carbon. *Nature*, *471*(7338), 349–352. https://doi.org/10.1038/nature09826

Shackleton, N. J. (1986). Paleogene stable isotope events. *Palaeogeography, Palaeoclimatology, Palaeoecology*, *57*(1), 91–102. https://doi.org/10.1016/0031-0182(86)90008-8

Shen, Y., & Benner, R. (2018). Mixing it up in the ocean carbon cycle and the removal of refractory dissolved organic carbon. *Scientific Reports*, *8*(1), 2542. https://doi.org/10.1038/s41598-018-20857-5

Sluijs, A., & Brinkhuis, H. (2009). A dynamic climate and ecosystem state during the Paleocene-Eocene thermal maximum: Inferences from dinoflagellate cyst assemblages on the New Jersey shelf. *Biogeosciences*, *6*(8), 1755–1781. https://doi.org/10.5194/bg-6-1755-2009

Sluijs, A., Brinkhuis, H., Schouten, S., Bohaty, S. M., John, C. M., Zachos, J. C., et al. (2007). Environmental precursors to rapid light carbon injection at the Palaeocene/Eocene boundary. *Nature*, *450*(7173), 1218–1221. https://doi.org/10.1038/nature06400

Sluijs, A., Fokkema, C. D., Agterhuis, T., Gerritsma, D., de Goeij, M., Liu, X., et al. (2024). Ocean drilling program site 959 datasets (1.1.0) [Dataset]. *Zenodo*. https://doi.org/10.5281/zenodo.13144797

Sluijs, A., Schouten, S., Donders, T. H., Schoon, P. L., Röhl, U., Reichart, G.-J., et al. (2009). Warm and wet conditions in the Arctic region during Eocene thermal maximum 2. *Nature Geoscience*, *2*(11), 777–780. https://doi.org/10.1038/ngeo668

Sluijs, A., van Roij, L., Frieling, J., Laks, J., & Reichart, G.-J. (2018). Single-species dinoflagellate cyst carbon isotope ecology across the Paleocene-Eocene Thermal Maximum. *Geology*, *46*(1), 79–82. https://doi.org/10.1130/G39598.1

Stockmarr, J. (1972). Tablets with spores used in absolute pollen analysis. *Pollen et Spores*, *13*, 615–621.

Svensen, H., Planke, S., Malthe-Sørenssen, A., Jamtveit, B., Myklebust, R., Rasmussen Eidem, T., & Rey, S. S. (2004). Release of methane from a volcanic basin as a mechanism for initial Eocene global warming. *Nature*, *429*(6991), 542–545. https://doi.org/10.1038/nature02566

Taylor, K. W. R., Huber, M., Hollis, C. J., Hernandez-Sanchez, M. T., & Pancost, R. D. (2013). Re-evaluating modern and Palaeogene GDGT distributions: Implications for SST reconstructions. *Global and Planetary Change*, *108*, 158–174. https://doi.org/10.1016/j.gloplacha.2013.06.011

Thöle, L. M., Nooteboom, P. D., Hou, S., Wang, R., Nie, S., Michel, E., et al. (2023). An expanded database of Southern Hemisphere surface sediment dinoflagellate cyst assemblages and their oceanographic affinities. *Journal of Micropalaeontology*, *42*(1), 35–56. https://doi.org/10.5194/jm-42-35-2023

Thomas, E., & Zachos, J. C. (2000). Was the late Paleocene thermal maximum a unique event? *GFF*, *122*(1), 169–170. https://doi.org/10.1080/11035890001221169

Tierney, J. E., Zhu, J., Li, M., Ridgwell, A., Hakim, G. J., Poulsen, C. J., et al. (2022). Spatial patterns of climate change across the Paleocene–Eocene thermal maximum. *Proceedings of the National Academy of Sciences*, *119*(42), e2205326119. https://doi.org/10.1073/pnas.2205326119

Torsvik, T. H., Van der Voo, R., Preeden, U., Mac Niocaill, C., Steinberger, B., Doubrovine, P. V., et al. (2012). Phanerozoic polar wander, palaeogeography and dynamics. *Earth-Science Reviews*, *114*(3–4), 325–368. https://doi.org/10.1016/j.earscirev.2012.06.007

Tuenter, E., Weber, S. L., Hilgen, F. J., & Lourens, L. J. (2003). The response of the African summer monsoon to remote and local forcing due to precession and obliquity. *Global and Planetary Change*, *36*(4), 219–235. https://doi.org/10.1016/S0921-8181(02)00196-0

Usup, G., Ahmad, A., Matsuoka, K., Lim, P. T., & Leaw, C. P. (2012). Biology, ecology and bloom dynamics of the toxic marine dinoflagellate Pyrodinium bahamense. *Harmful Algae*, *14*, 301–312. https://doi.org/10.1016/j.hal.2011.10.026

Vallé, F., Westerhold, T., & Dupont, L. M. (2017). Orbital-driven environmental changes recorded at ODP site 959 (eastern equatorial Atlantic) from the late Miocene to the early Pleistocene. *International Journal of Earth Sciences*, *106*(3), 1161–1174. https://doi.org/10.1007/s00531-016-1350-z

van der Weijst, C. M. H., van der Laan, K. J., Peterse, F., Reichart, G.-J., Sangiorgi, F., Schouten, S., et al. (2022). A 15-million-year surface- and subsurface-integrated TEX_{86} temperature record from the eastern equatorial Atlantic. *Climate of the Past*, *18*(8), 1947–1962. https://doi.org/10.5194/cp-18-1947-2022

van Hinsbergen, D. J. J., de Groot, L. V., van Schaik, S. J., Spakman, W., Bijl, P. K., Sluijs, A., et al. (2015). A paleolatitude calculator for paleoclimate studies. *PLoS One*, *10*(6), e0126946. https://doi.org/10.1371/journal.pone.0126946

Wagner, T. (2002). Late Cretaceous to early Quaternary organic sedimentation in the eastern equatorial Atlantic. *Palaeogeography, Palaeoclimatology, Palaeoecology*, *179*(1–2), 113–147. https://doi.org/10.1016/S0031-0182(01)00415-1

Weedon, G. P., Shackleton, N. J., & Pearson, P. N. (1997). The Oligocene time scale and cyclostratigraphy on the Ceara rise, Western equatorial Atlantic. *Proceedings of the Ocean Drilling Program, Scientific Results*, *154*, 101–114. https://doi.org/10.2973/odp.proc.sr.154.1997

Westerhold, T., Marwan, N., Drury, A. J., Liebrand, D., Agnini, C., Anagnostou, E., et al. (2020). An astronomically dated record of Earth's climate and its predictability over the last 66 million years. *Science*, *369*(6509), 1383–1387. https://doi.org/10.1126/science.aba6853

Westerhold, T., Röhl, U., Donner, B., & Zachos, J. C. (2018). Global extent of early Eocene hyper thermal events: A new Pacific benthic foraminiferal isotope record from Shatsky rise (ODP site 1209). *Paleoceanography and Paleoclimatology*, *33*(6), 626–642. https://doi.org/10.1029/2017PA003306

Westerhold, T., Röhl, U., Frederichs, T., Agnini, C., Raffi, I., Zachos, J. C., & Wilkens, R. H. (2017). Astronomical calibration of the Y Persian timescale: Implications for seafloor spreading rates and the chaotic behavior of the solar system? *Climate of the Past*, *13*(9), 1129–1152. https://doi.org/10.5194/cp-13-1129-2017

Westerhold, T., Röhl, U., Pälike, H., Wilkens, R., Wilson, P. A., & Acton, G. (2014). Orbitally tuned timescale and astronomical forcing in the middle Eocene to early Oligocene. *Climate of the Past*, *10*(3), 955–973. https://doi.org/10.5194/cp-10-955-2014

Willard, D. A., Donders, T. H., Reichgelt, T., Greenwood, D. R., Sangiorgi, F., Peterse, F., et al. (2019). Arctic vegetation, temperature, and hydrology during Early Eocene transient global warming events. *Global and Planetary Change*, *178*, 139–152. https://doi.org/10.1016/j.gloplacha.2019.04.012

Williams, G. L., Fensome, R. A., & MacRae, R. A. (2017). *The Lentin and Williams index of Fossil dinoflagellates 2017 edition*. American Association of Stratigraphic Palynologists foundation.

Wubben, E., Spiering, B. R., Veenstra, T., Bos, R., Wang, Z., Van Dijk, J., et al. (2024). Tropical warming and intensification of the West African monsoon during the Miocene climatic Optimum. *Paleoceanography and Paleoclimatology*, *39*(5), e2023PA004767. https://doi.org/10.1029/2023PA004767

Wubben, E., Veenstra, T., Witkowski, J., Raffi, I., Hilgen, F., Bos, R., et al. (2023). Astrochronology of the Miocene climatic optimum record from Ocean Drilling program site 959 in the eastern equatorial Atlantic. *Newsletters on Stratigraphy*, *56*(4), 457–484. https://doi.org/10.1127/nos/2023/0749

Zachos, J. C., McCarren, H., Murphy, B., Röhl, U., & Westerhold, T. (2010). Tempo and scale of late Paleocene and early Eocene carbon isotope cycles: Implications for the origin of hyperthermals. *Earth and Planetary Science Letters*, *299*(1–2), 242–249. https://doi.org/10.1016/j.epsl.2010.09.004

Zeeden, C., Hilgen, F., Röhl, U., Seelos, K., & Lourens, L. (2015). Sediment color as a tool in cyclostratigraphy – A new application for improved data acquisition and correction from drill cores. *Newsletters on Stratigraphy*, *48*(3), 277–285. https://doi.org/10.1127/nos/2015/0064

Zhang, Y., Boer, A. M., Lunt, D. J., Hutchinson, D. K., Ross, P., Flierdt, T., et al. (2022). Early Eocene ocean meridional overturning Circulation: The roles of atmospheric forcing and strait geometry. *Paleoceanography and Paleoclimatology*, *37*(3), e2021PA004329. https://doi.org/10.1029/2021PA004329

Zhang, Y. G., Pagani, M., & Wang, Z. (2016). Ring index: A new strategy to evaluate the integrity of TEX 86 paleothermometry. *Paleoceanography*, *31*(2), 220–232. https://doi.org/10.1002/2015PA002848

Zonneveld, K. A. F., Marret, F., Versteegh, G. J. M., Bogus, K., Bonnet, S., Bouimetarhan, I., et al. (2013). Atlas of modern dinoflagellate cyst distribution based on 2405 data points. *Review of Palaeobotany and Palynology*, *191*, 1–197. https://doi.org/10.1016/j.revpalbo.2012.08.003

References From the Supporting Information

Blaga, C. I., Reichart, G.-J., Heiri, O., & Sinninghe Damsté, J. S. (2009). Tetraether membrane lipid distributions in water-column particulate matter and sediments: A study of 47 European lakes along a north south transect. *Journal of Paleolimnology*, *41*(3), 523–540. https://doi.org/10.1007/s10933-008-9242-2

O'Brien, C. L., Robinson, S. A., Pancost, R. D., Sinninghe Damsté, J. S., Schouten, S., Lunt, D. J., et al. (2017). Cretaceous sea-surface temperature evolution: Constraints from TEX_{86} and planktonic foraminiferal oxygen isotopes. *Earth-Science Reviews*, *172*, 224–247. https://doi.org/10.1016/j.earscirev.2017.07.012

Weijers, J. W. H., Lim, K. L. H., Aquilina, A., Sinninghe Damsté, J. S., & Pancost, R. D. (2011). Biogeochemical controls on glycerol dialkyl glycerol tetraether lipid distributions in sediments characterized by diffusive methane flux. *Geochemistry, Geophysics, Geosystems*, *12*(10), Q10010. https://doi.org/10.1029/2011GC003724

Zhang, Y. G., Zhang, C. L., Liu, X.-L., Li, L., Hinrichs, K.-U., & Noakes, J. E. (2011). Methane index: A tetraether archaeal lipid biomarker indicator for detecting the instability of marine gas hydrates. *Earth and Planetary Science Letters*, *307*(3–4), 525–534. https://doi.org/10.1016/j.epsl.2011.05.031